

Characterization of breast calcification types using dual energy X-ray method

This content has been downloaded from IOPscience. Please scroll down to see the full text.

Download details:

IP Address: 128.41.35.156

This content was downloaded on 14/08/2017 at 14:31

Manuscript version: Accepted Manuscript

Martini et al

To cite this article before publication: Martini et al, 2017, Phys. Med. Biol., at press:

<https://doi.org/10.1088/1361-6560/aa8445>

This Accepted Manuscript is: © 2017 Institute of Physics and Engineering in Medicine

During the embargo period (the 12 month period from the publication of the Version of Record of this article), the Accepted Manuscript is fully protected by copyright and cannot be reused or reposted elsewhere.

As the Version of Record of this article is going to be / has been published on a subscription basis, this Accepted Manuscript is available for reuse under a CC BY-NC-ND 3.0 licence after the 12 month embargo period.

After the embargo period, everyone is permitted to copy and redistribute this article for non-commercial purposes only, provided that they adhere to all the terms of the licence

<https://creativecommons.org/licences/by-nc-nd/3.0>

Although reasonable endeavours have been taken to obtain all necessary permissions from third parties to include their copyrighted content within this article, their full citation and copyright line may not be present in this Accepted Manuscript version. Before using any content from this article, please refer to the Version of Record on IOPscience once published for full citation and copyright details, as permission will likely be required. All third party content is fully copyright protected, unless specifically stated otherwise in the figure caption in the Version of Record.

When available, you can view the Version of Record for this article at:

<http://iopscience.iop.org/article/10.1088/1361-6560/aa8445>

Characterization of breast calcification types using dual energy X-ray method

N Martini¹, V Koukou¹, G Fountos², C Michail², A Bakas³, I Kandarakis², R Speller⁴, G Nikiforidis¹

¹ Department of Medical Physics, Medical School, University of Patras, 265 00 Patras, Greece

² Radiation Physics, Materials Technology and Biomedical Imaging Laboratory, Department of Biomedical Engineering, Technological Educational Institute of Athens, Egaleo, 122 10 Athens, Greece

³ Department of Radiology & Radiation Therapy, Faculty of Health and Caring Professions, Technological Educational Institution of Athens, 122 10 Athens, Greece

⁴ Department of Medical Physics and Bioengineering, University College London, Malet Place, Gower Street, London WC1E 6BT, UK

E-mail: George Fountos, gfoun@teiath.gr

Abstract. Calcifications are products of mineralization whose presence is usually associated with pathological conditions. The minerals mostly seen in several diseases are calcium oxalate (CaC_2O_4), calcium carbonate (CaCO_3) and hydroxyapatite (HAp). Up to date, there is no *in-vivo* method that could discriminate between minerals. To this aim, a dual energy X-ray method was developed in the present study. An analytical model was implemented for the determination of the Calcium/Phosphorus mass ratio ($m_{\text{Ca}}/m_{\text{P}}$). The simulation was carried out using monoenergetic and polyenergetic X-rays and various calcification thicknesses (100 to 1000 μm) and types (CaC_2O_4 , CaCO_3 , HAp). The experimental evaluation of the method was performed using the optimized irradiation conditions obtained from the simulation study. X-ray tubes, combined with energy dispersive and energy integrating (imaging) detectors, were used for the determination of the $m_{\text{Ca}}/m_{\text{P}}$ in phantoms of different mineral types and thicknesses. Based on the results of the experimental procedure, statistical significant difference was observed between the different types of minerals when calcification thicknesses were 300 μm or higher.

Keywords: Dual energy, calcifications, calcium/phosphorus ratio

1. Introduction

Breast cancer is the most common cause of cancer deaths, accounting for approximately 16% in adult women (WHO 2008). Early detection is important for patients' treatment and

1
2
3
4
5
6
7
8
9
10
11
12
13
14
15
16
17
18
19
20
21
22
23
24
25
26
27
28
29
30
31
32
33
34
35
36
37
38
39
40
41
42
43
44
45
46
47
48
49
50
51
52
53
54
55
56
57
58
59
60

recovery. Preliminary signs of masses and microcalcifications are important indicators of breast cancer (Roberts *et al* 1995, Kappadath and Shaw 2004, 2005). A significant percentage of non-palpable breast cancers (30-50%) are detected only due to the appearance of microcalcifications in a mammogram (Cox and Morgan 2013). Several studies have suggested that the presence of calcifications may also be of biological significance, while its type may indicate malignancy and disease state (Radi 1989, Morgan *et al* 2001, 2005).

Microcalcifications of the breast were firstly described as calcium deposits within the breast tissue (Leborgne 1951). The three main compositions described in literature are hydroxyapatite (HAp), calcium oxalate (CaC_2O_4) and calcium carbonate (CaCO_3) (Fandos-Morera *et al* 1988, Chen *et al* 2008). Microcalcifications are divided into Type I and Type II. Type I calcifications are composed of calcium oxalate (CaC_2O_4), and are associated with benign lesions of the breast or at most non-invasive lobular carcinoma in situ (Busing *et al* 1981, Frappart *et al* 1986). Type II calcifications are composed of calcium phosphate, mainly hydroxyapatite (HAp), and are associated with malignant breast conditions (Haka *et al* 2002) including carcinomas (Frappart *et al* 1984). Furthermore, calcifications composed of calcium carbonate (CaCO_3) are associated with benign lesions of the breast (Fandos-Morera *et al* 1988, Baker *et al* 2007). It is often the presence of Type II calcifications that leads to further investigations (Baker *et al* 2010, Kerssens *et al* 2010), and they are estimated to occur two to three times more frequently than Type I (Haka *et al* 2002).

Mammography is considered as the most reliable method in detection of breast calcifications (Haka *et al* 2002). A major limitation in mammography is the low contrast between glandular and pathologic tissue (Johns and Yaffe 1987, Byng *et al* 1998), which have similar composition. Dual energy techniques (DE) are able to cancel out the tissue background structures and highlight specific lesions (Taibi *et al* 2003, Kappadath and Shaw 2004, 2005, 2008, Chen *et al* 2013, Del Lama 2016, 2016a, Koukou *et al* 2017). However, both mammography and DE techniques are not able to yield information about the chemical composition of calcifications and help in classifying benign and malignant lesions. Previous noninvasive investigations, using Raman spectroscopy, discriminated malignant and benign lesions in penetration depths from 0.96 to 27 mm (Baker *et al* 2007, Matousek and Stone 2007, Stone *et al* 2007, Stone and Matousek 2008, Matousek and Stone 2013). More recently, a method using X-ray phase-contrast imaging was proposed, based on the absorption and small-angle scattering signals of the different types of microcalcifications (Wang *et al* 2014).

In the present study a dual energy method was developed for the characterization of calcification minerals, based on the determination of Calcium/Phosphorus mass ratio ($m_{\text{Ca}}/m_{\text{P}}$). For the minerals, where the Phosphorus is absent, an effective $m_{\text{Ca}}/m_{\text{P}}$ was defined. A simulation study, based on analytical modeling was performed using monoenergetic and polyenergetic X-rays in order to obtain the optimized irradiation parameters. Experimental evaluation of the method was followed using photon counting energy dispersive and energy integrating detectors. Results are presented and used to discuss and demonstrate the feasibility of using $m_{\text{Ca}}/m_{\text{P}}$ as a parameter for minerals discrimination.

2. Materials and methods

2.1. Simulation studies

2.1.1. Monoenergetic beams

The attenuated intensities for the low-/high-energy beams were calculated through analytical modeling according to the following procedure. Consider that along the monoenergetic X-ray path, a compressed breast of thickness, T , is composed of: (i) 50% adipose and 50% glandular tissue (breast tissue) of thickness t_b and (ii) a calcification of thickness t_c (figure 1).

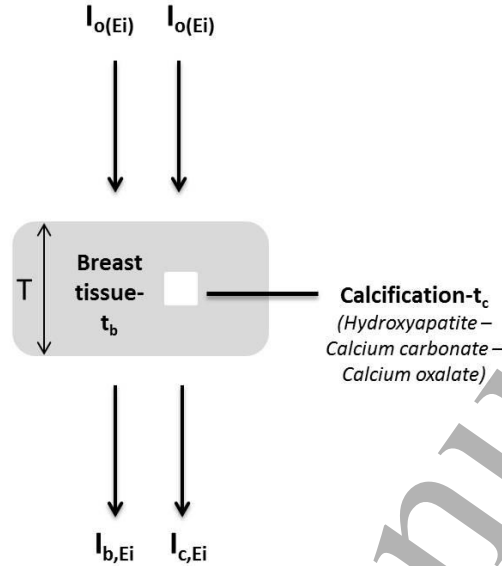


Figure 1. Schematic representation of the procedure for calculating the attenuated intensities I_{b,E_i} and I_{c,E_i} .

Under this consideration, when the X-ray beam passes through only breast tissue, the low-/high-energy intensities, I_{b,E_l} and I_{b,E_h} , are calculated by:

$$I_{b,E_i} = I_{o,E_i} e^{-\mu_{b,E_i} T} \quad i = l, h \quad (1)$$

When the beam passes through the breast tissue and the calcification (minerals), the low-/high-energy attenuated intensities, I_{c,E_l} and I_{c,E_h} , can be expressed as:

$$I_{c,E_i} = I_{o,E_i} e^{-\mu_{b,E_i} t_b - \mu_{mineral,E_i} t_c} \quad i = l, h \quad (2)$$

where, I_{o,E_l} and I_{o,E_h} are the unattenuated low-/high-energy intensities. The energy-dependent linear attenuation coefficients (cm^{-1}) and thicknesses (cm) for breast tissue and minerals are given by μ_{b,E_i} , $\mu_{mineral,E_i}$ and t_b , t_c respectively.

Three different types of calcifications (minerals) were examined: (i) hydroxyapatite, HAp, $(\text{Ca}_{10}(\text{PO}_4)_6(\text{OH})_2)$ with density of 3.18 g/cm^3 (Gong *et al* 1964), (ii) calcium carbonate (CaCO_3) with density of 2.93 g/cm^3 (Lemacks *et al* 2002), and (iii) calcium oxalate (CaC_2O_4) with density of 2.20 g/cm^3 (Brandan and Ramirez 2006). The minerals are referred to as HAp, CaCO_3 and CaC_2O_4 .

The unattenuated low-/high-energy intensities I_{o,E_l} and I_{o,E_h} were calculated through the

entrance surface dose (K_a) (Eq. 3) for photon energies between 15 and 70 keV at a resolution of 1 keV, following Eq. 4.

$$K_a(mGy) = 8.77 \cdot 10^{-3} \cdot 1.83 \cdot 10^{-6} I_{o,E_i} E_i \left(\frac{\mu_{en}}{\rho} \right)_{air} \quad (3)$$

$$I_{o,E_i} = \frac{K_a(mGy)}{8.77 \cdot 10^{-3} \cdot 1.83 \cdot 10^{-6} E_i \left(\frac{\mu_{en}}{\rho} \right)_{air}} \quad (4)$$

where I_{o,E_i} is the unattenuated intensity (photons/mm²) at energy E_i . $(\mu_{en}/\rho)_{E_i}$ is the X-ray mass energy absorption coefficient of air at energy E_i obtained from the literature (Hubbell and Seltzer 1996). K_a was set at 6 mGy and was split evenly between the low-/high-energy (European Commission 2014).

The attenuated intensities, I_{b,E_i} and I_{c,E_i} , were calculated using mass attenuation coefficients from published data (NIST) (Hubbell and Seltzer 1996). The mass attenuation coefficients were multiplied by the corresponding densities for each material in order to obtain the energy-dependent linear attenuation coefficients. In our method, the input data for the mineral characterization are the attenuated intensities of minerals and the surrounding soft tissue. In practice, for a given attenuated intensity after breast exposure, different mineral types must be distinguished. In order this study to be more realistic, in both computer simulation and experimental studies, for every HAp thickness the equivalent thicknesses of calcite and calcium oxalate were defined resulting in equal attenuation. Warren *et al* 2013 also concluded in this approach, in order to preserve equivalent attenuation and contrast in the mammographic image (Warren *et al* 2013). The calcification HAp thicknesses (t_c) ranged from 100 to 1000 μm , at 50 μm increments. The corresponding thicknesses of calcite and calcium oxalate were calculated for all examined energies, in order the number of photons after attenuation (I_{c,E_i}) to be equal. Then, the thicknesses for all energies were averaged for calcite and calcium oxalate, resulting in standard deviation (SD) lower than 20.87 μm . The HAp thicknesses and the corresponding thicknesses for CaCO_3 and CaC_2O_4 are presented in table 1. The total breast thickness (T) was 4.2 cm (ACR 2006).

Table 1. Examined calcification thicknesses of HAp, CaCO_3 and CaC_2O_4 .

Calcification thicknesses, t_c (μm)					
Hap	CaCO_3	CaC_2O_4	Hap	CaCO_3	CaC_2O_4
100	123.72	208.49	600	742.30	1250.97
150	185.57	312.74	650	804.15	1355.21
200	247.29	416.99	700	866.01	1459.46
250	309.29	521.24	750	927.87	1563.71
300	371.15	625.48	800	989.73	1667.95
350	433.01	729.73	850	1051.58	1772.20
400	494.86	833.98	900	1113.44	1876.45
450	556.72	938.22	950	1175.30	1980.69

500	618.58	1040.47	1000	1237.16	2084.94
550	680.44	1146.72			

The m_{Ca}/m_P was then calculated for each calcification type, using Eq. A19 (please see Appendix). Note that hydroxyapatite indicated malignancy, whereas calcite and calcium oxalate are indicators of benign calcifications. When malignant calcifications are present, the model estimates the m_{Ca}/m_P of hydroxyapatite where Ca and P are both elements in this molecule. On the contrary, P is not present in benign calcifications ($CaCO_3$, CaC_2O_4). In this case, the model calculates an effective m_{Ca}/m_P . In this method, where an unknown calcification type must be characterized by attenuation intensity measurements, the calculation of m_{Ca}/m_P uses the linear attenuation coefficients of PO_4 for all calcification types. The notation of 'effective' m_{Ca}/m_P was introduced, since an amount of CO_3 or C_2O_4 corresponds to a smaller amount of PO_4 , in order to preserve equal photon beam attenuation. This is due to the lower linear attenuation coefficients of carbonate and oxalate compared to phosphate. Thus, m_{Ca}/m_P as calculated by Eq. A19 (please see Appendix) is expected to be lower for mineral types without phosphorus present in their molecule.

The coefficient of variation of the m_{Ca}/m_P ($CV_{m_{Ca}/m_P}(\%)$) was calculated using Eq. A20 (please see Appendix) for each calcification type. The selection of the optimum energy pair was based on the minimization of the $CV_{m_{Ca}/m_P}(\%)$. The $CV_{m_{Ca}/m_P}(\%)$ of each mineral is referred to as $CV_{m_{Ca}/m_P,HAp}(\%)$, $CV_{m_{Ca}/m_P,CaCO_3}(\%)$ and $CV_{m_{Ca}/m_P,CaC_2O_4}(\%)$ for HA_p, $CaCO_3$ and CaC_2O_4 , respectively.

2.1.2. Polyenergetic X-rays

In order to obtain spectra with mean energies similar to those employed in the monoenergetic study, two different configurations were evaluated: (i) irradiation with the single exposure technique, and (ii) irradiation with the double exposure technique. For the implementation of the method using polyenergetic spectra, the linear attenuation coefficients were replaced by effective linear attenuation coefficients in Eqs. 1 and 2.

Unfiltered spectra were obtained from TASMIP spectral models generated for Tungsten (W) anode (Boone and Siebert 1997). The breast composition and thickness, as well as, the used calcification types and thicknesses were the same to those of the monoenergetic study.

2.1.2.1. Single exposure

In the single exposure technique, an appropriate filter was placed in the beam path (Sotiropoulou *et al* 2015, 2016). Filters with appropriate K-absorption edges were applied, in order to modify the X-ray spectrum in two well-separated energy bands with mean energies as indicated by the monoenergetic study (Koukou *et al* 2015, Martini *et al* 2015). Therefore, Rhodium (Rh), Palladium (Pd), Silver (Ag), Cadmium (Cd), Tin (Sn) and Iodine (I) filters with K-edges of 23.22 keV, 24.35 keV, 25.51 keV, 26.71 keV, 29.20 keV and 33.17 keV, respectively, were applied at tube voltage of 70 kV. The filter thicknesses ranged from 100 to 1000 μm at 50 μm increments. The unfiltered spectrum was obtained for 300 mAs, corresponding to a 5 minutes measurement with a Norland XR-46 (Norland Medical Systems

Inc., Fort Atkinson, WI) W anode X-ray source, operating at 70 kV with a 1 mA current. An ionization chamber (Radcal 2026C) was positioned at a distance of 66 cm from the tube output and an entrance surface dose of 101.03 mGy was measured.

2.1.2.2. Double exposure

In the double exposure method, two separate images are acquired at two different kVs (Sorenson *et al* 1989). In order to obtain low-/high-energy spectra with mean energies similar to those indicated by the monoenergetic study, a radiographic unit with W anode is required. Commercially available radiographic units operate in the range from 40 to 150 kV, while mammographic units cannot be used since the tube does not exceed 50 kV. In a previous simulation study by our group, various filter materials and thicknesses, for the modification of the low-energy spectrum, were examined. Best results were obtained for the 100 μm Cd filtered spectrum at 40 kV, since this filter provided narrower spectra with adequate number of photons (Koukou *et al* 2015). For the modification of the high-energy spectrum, Copper (Cu), Holmium (Ho), Thulium (Tm) and Lutetium (Lu) filters were examined at 70 kV for thicknesses in the range of 500 to 1500 μm at 100 μm increments. Copper is a commonly used low cost filter in X-ray systems since it attenuates the low energies in spectra. Ho, Tm and Lu are lanthanide filters with K-edges of 55.59 keV, 59.37 keV and 63.31 keV, respectively. The filters for the low-/high-energy were applied to unfiltered spectra obtained at 400 and 250 mAs, respectively. The 400 mAs value for the low-energy was the maximum that could be obtained, while the 250 mAs for the high-energy is a high value. An ionization chamber (Radcal 2026C) was positioned at 66 cm from the tube output and entrance surface doses of 11.32 and 28.90 mGy were measured for the low- and high-energy, respectively.

2.1.3. Nonparametric statistical analysis

A statistical analysis was conducted using the polyenergetic X-rays. Assuming Poisson distribution for the attenuated intensities (I_{b,E_i} and I_{c,E_i}), 5000 random values were generated for I_{b,E_i} and I_{c,E_i} . Thus, 5000 $m_{\text{Ca}}/m_{\text{P}}$ values were calculated using Eq. A19 (please see Appendix), for each calcification type (HAp, CaCO_3 , CaC_2O_4) and thickness. A statistical analysis was then followed to define the distribution that describes the random variable ($m_{\text{Ca}}/m_{\text{P}}$) in each examined case. To this aim, nonparametric statistical methods were used, since the distribution of the random variable $m_{\text{Ca}}/m_{\text{P}}$ is unknown. The one-sample Kolmogorov-Smirnov and chi-square tests were used with significance level set at 5%. The normal Kernel distribution (Eq. 5) was applied to the data of the random variable $m_{\text{Ca}}/m_{\text{P}}$ as the p-value was higher than 0.05 in all cases.

$$f(x) = \frac{1}{Nh} \sum_{i=1}^N \frac{1}{\sqrt{2\pi}} e^{-\frac{1}{2} \left(\frac{x-x_i}{h} \right)^2}, \quad N = 5000 \quad (5)$$

where N is the sample size, x_i are the values of the random variable $m_{\text{Ca}}/m_{\text{P}}$, and h is the bandwidth. The bandwidth controls the smoothness of Kernel function, because it determines

1
2
3 how the probability associated with each observation is spread over the surrounding sample
4 (Bowman and Azzalini 1997). There are a number of techniques that automatically choose the
5 bandwidth (Jones *et al* 1996). In the current study, the 'fitdist' routine of Matlab R2017a was
6 used to obtain the Kernel distribution and the bandwidth.

7
8 The Kernel probability functions were produced for all calcification types and thicknesses.
9 The probability distribution functions obtained from HAp were plotted together with the
10 corresponding functions of CaCO_3 and CaC_2O_4 . The false negative and false positive values
11 were calculated from the probability distribution functions.

12
13 The nonparametric statistical analysis was also conducted for breast thicknesses of 5 and 6
14 cm, in order to investigate the influence of breast thickness on the false negative and false
15 positive values.
16

17 18 2.2. Experimental evaluation of the method

19 2.2.1. Calcification phantoms

20
21 For the evaluation of the method, twelve different calcification phantoms were constructed:
22 four HAp thicknesses and the corresponding thicknesses of calcite and calcium oxalate (4
23 thicknesses \times 3 minerals = 12 phantoms). The HAp thicknesses were 300, 500, 700, 900 μm
24 and the corresponding thicknesses of calcite and calcium oxalate are shown in table 1. The
25 materials used in this study, were hydroxyapatite (FLUKA 21223, $\geq 90\%$ purity), calcium
26 carbonate (CAS Nr: 207-439-9, $\geq 99\%$ purity), calcium oxalate (CAS Nr: 563-72-4, 99.99%
27 purity) and deionized water. Polymethyl methacrylate (PMMA) tubes, with an outer diameter
28 of 2 cm and length of 3 cm, were filled with a mixture of the aforementioned materials and
29 double distilled water (figure 2). The cylinder phantoms were sealed in both top and bottom
30 with 0.5 mm PMMA discs. A vacuum tube was used to diminish the remaining air in the
31 phantoms. Each phantom was immersed in a cubic PMMA tank ($10 \times 10 \times 10 \text{ cm}^3$), filled with
32 water (4.2 cm thickness), simulating the average breast. Two PMMA discs, with equal
33 dimensions as those used for the sealed cylinder phantoms, were placed in the beam path
34 when measurements without the cylinder phantoms were performed.
35
36
37
38
39
40

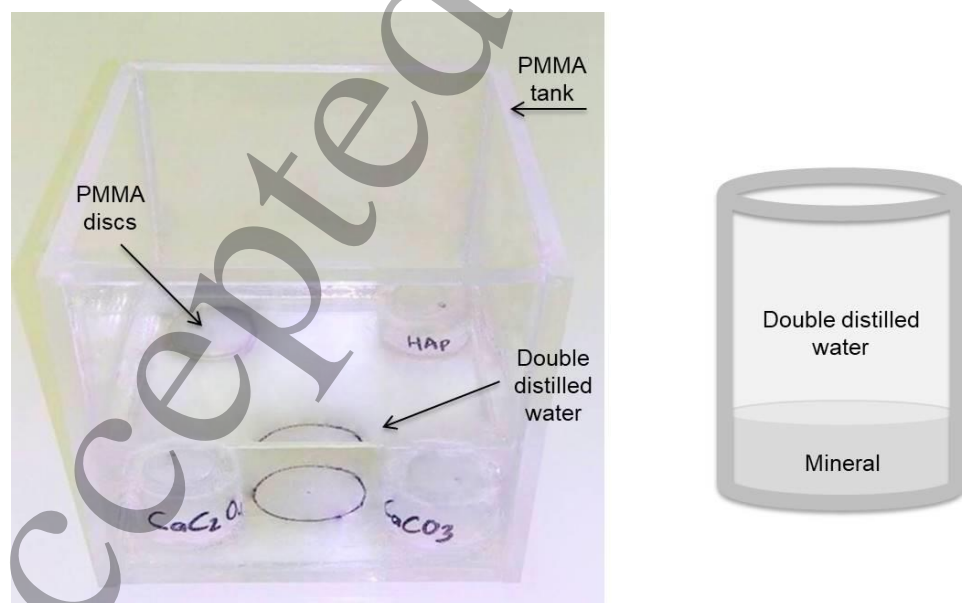


Figure 2. Photo of the tank with the immersed calcification phantoms (left) and schematic representation of the phantom (right).

2.2.2. Single exposure technique

The X-ray source was a tungsten (W) anode Norland XR-46 (Norland Medical Systems Inc., Fort Atkinson, WI) operating at 60 to 100 kV and 0.05 to 1 mA current. Appropriate collimation (1 mm radius) was applied, in order to obtain a narrow pencil beam, resulting in limited scatter contribution to the spectra. The inherent Samarium filter employed by Norland was extracted and replaced by 300 μm Cd, as indicated by the simulation study. A tube current of 0.5 mA was used in the measurements. A Cadmium Telluride (CdTe) X-ray energy discriminating and counting system (AMPTTEK XR-100T) was used (Michail *et al* 2011a, 2011b). The digital processor was the PX4. The energy calibration of the detection system was performed using ^{125}I and $^{99\text{m}}\text{Tc}$ γ -ray calibration sources (Martini *et al* 2015). The measured X-ray spectra were corrected for both the CdTe detector efficiency and the dead time of the digital processor (Sotiropoulou *et al* 2015). The selected low-energy band consisted of energies in the range of 23.04 to 26.99 keV, while the high-energy band was in the range of 50.10 to 64.06 keV. Two sequential measurements were obtained using the constructed phantoms, the first with only the water in the radiation path, and the second with the calcification phantom along the radiation path and immersed in the water tank. In both measurements, the total thickness was kept constant and equal to 4.2 cm. The acquisition time was 5 minutes. Ten repeated measurements were obtained in order to determine the $m_{\text{Ca}}/m_{\text{P}}$ and the coefficient of variation of the measurements ($CV_{m_{\text{Ca}}/m_{\text{P}},\text{meas}}(\%) = SD_{m_{\text{Ca}}/m_{\text{P}}} / \text{mean}_{m_{\text{Ca}}/m_{\text{P}}}$). The experimental configuration is shown in figure 3.

2.2.3. Double exposure technique

The Del Medical Eureka W anode radiographic system was used with added filtration of 100 μm Cd (Alfa Aesar 11371, 99.9975%) at 40 kV, 400 mAs and 1000 μm Cu (PTW 99.99%) at 70 kV, 250 mAs for the low- and high-energy spectra, respectively (Koukou *et al* 2017a). The detection system was a terbium-doped gadolinium oxysulfide ($\text{Gd}_2\text{O}_2\text{S:Tb}$) phosphor screen (Min-R 2190 with mass thickness of 33.91 mg/cm^2) coupled to an optical readout device including a complementary metal-oxide-semiconductor (CMOS) Remote RadEye HR photodiode pixel array. The CMOS photodiode array has a format of 1200 \times 1600 pixels, corresponding to an active area of 27 mm \times 36 mm, with a pixel pitch of 22.5 μm . The $\text{Gd}_2\text{O}_2\text{S:Tb}$ screen was directly overlaid onto the active area of the CMOS (no fiber optic plate or coupling gel were used) (Michail *et al* 2011b). The source-to-detector distance (SDD) was set at 66 cm.

Since for the determination of $m_{\text{Ca}}/m_{\text{P}}$ the total number of photons (i.e. I_{b,E_i} , I_{c,E_i}) is required, the pixel values of the low- and high-energy images should be converted to photons. The detector response curve was measured in order to convert pixel values to dose and in turn, with known I_{b,E_i} , I_{c,E_i} spectra, to photons using Eq. 3 rewritten as follows (Koukou *et al* 2015):

$$K_a(mGy) = 8.77 * 10^{-3} \sum_{E_{min}}^{E_{max}} 1.83 * 10^{-6} I_{E_i} E_i \left(\frac{\mu_{en}}{\rho E_i} \right)_{air} \quad (6)$$

A PMMA tank filled with water of 4.2 cm total thickness, was positioned at 61.8 cm (source to object distance, SOD) from the tube exit and exposed using tube voltages of 40 and 70 kV for the low- and high-energy, respectively (Koukou *et al* 2015). The SDD was 66 cm. The experimental configuration is shown in figure 3. An ionization chamber (Radcal 2026C) was positioned at the surface of the breast phantom. The entrance surface air kerma was measured for a range of tube current-time products. Both LE and HE images were saved as 16 bit and 100x100 pixels square regions of interest (ROIs) were measured from each image. The mean pixel value (MPV) and the standard deviation within that region were measured and the relationship between MPV and the detector entrance dose was determined using linear regression (figure 4).

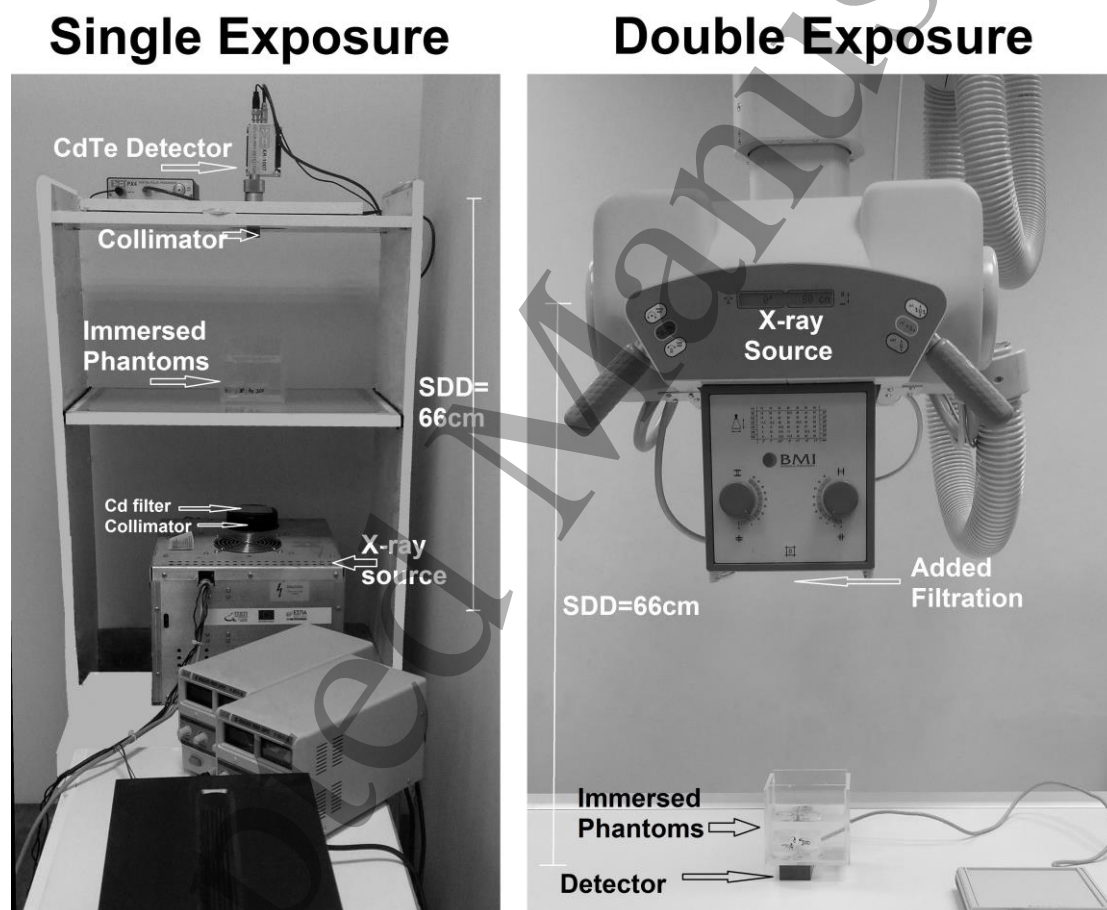


Figure 3. Experimental configuration for single and double exposure techniques.

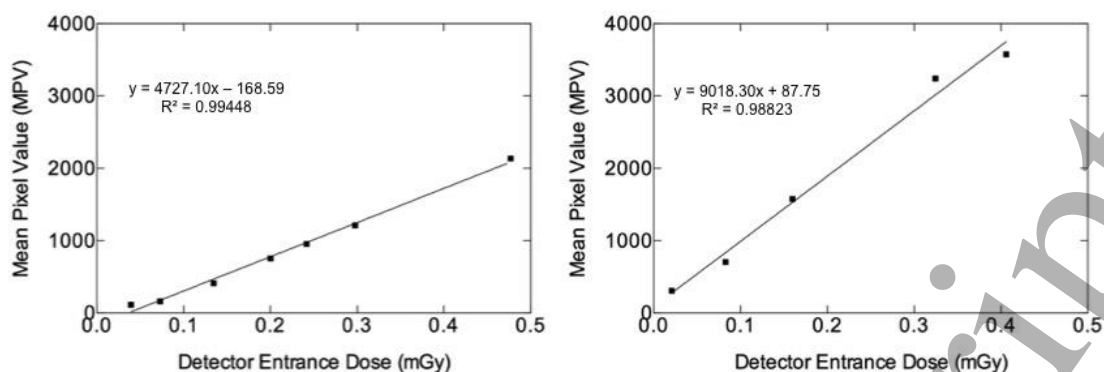


Figure 4. MPV as a function of the detector entrance dose for the low (left)-and high-energy (right).

Five low and five high-energy images were acquired for each calcification phantom in order to determine the m_{Ca}/m_P and the coefficient of variation ($CV_{m_{Ca}/m_P, meas} (\%) = SD_{m_{Ca}/m_P} / mean_{m_{Ca}/m_P}$). Between acquisitions, of each pair of low and high-energy images, the phantoms were repositioned. The phantom images were acquired with the irradiation conditions mentioned above and saved as 16 bit. Twenty ROIs of 44x44 pixels were selected in each image and the MPVs were converted into photons for the estimation of the m_{Ca}/m_P . In order to convert the MPV into number of photons, the measured 100 μm Cd and 1000 μm Cu filtered spectra, by the AMPTEK CdTe spectrometer, were used for the low- and high-energy, respectively (figure 5). The detector system was calibrated for energy scales, linearity checks and energy resolution, by using ^{125}I and $^{99\text{m}}\text{Tc}$ γ -ray calibration sources (Martini *et al* 2015).

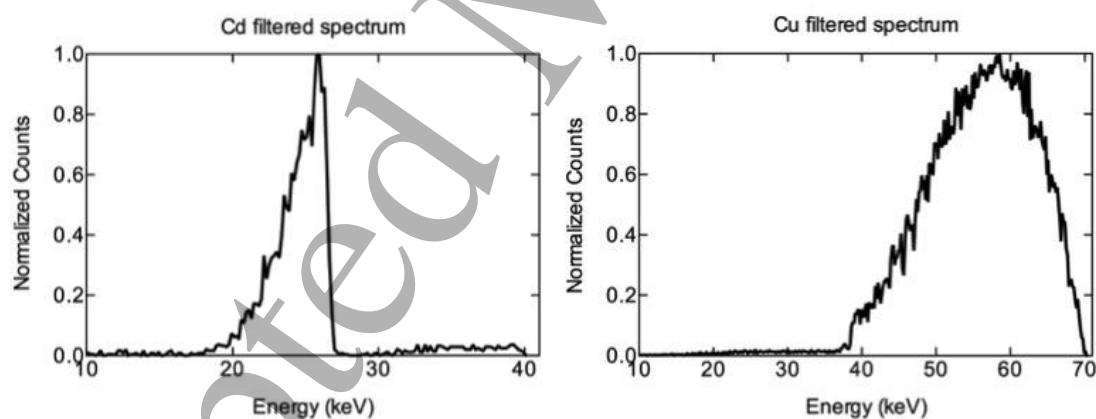


Figure 5. The 100 μm Cd and 1000 μm Cu filtered spectra for the low- and high-energy, respectively.

2.2.4. Statistical analysis

Since m_{Ca}/m_P probability distribution is not Gaussian, the Mann-Whitney U non-parametric statistical test was applied to the measured m_{Ca}/m_P values, in order to assess statistical significant difference between the different types of the examined minerals (Milton 1964). The Mann-Whitney U test is similar to t-test for the determination of statistical separation of two populations; however, it does not assume any specific distribution of the

data, unlike the t-test where a normal distribution is prerequisite (Milton 1964). All tests were two-tailed and the significance level was set at 5%.

3. Results

3.1. Simulation studies

3.1.1. Monoenergetic beams

Figure 6 shows the $CV_{mCa/mp}$ (%) of each mineral type and thickness as a function of low- and high-energy combinations. In this figure the $CV_{mCa/mp}$ (%) values ranged from the minimum $CV_{mCa/mp}$ (%) value, obtained in each case, up to +50% of the minimum $CV_{mCa/mp}$ (%), as calculated by Eq. A19. The ‘fit’ routine of Matlab R2017a was used for the presented surface plot. The indicative thicknesses presented are 100, 500 and 1000 μm of HAp and the corresponding thicknesses of CaCO_3 and CaC_2O_4 shown in table 1. In this study, the selected energy combinations were those resulting in 20% (or less) of the minimum $CV_{mCa/mp}$ (%). This criterion is fulfilled for every energy combination that can be obtained when the low-energy ranges from 23 to 27 keV and the high-energy ranges from 53 to 70 keV, for all minerals.

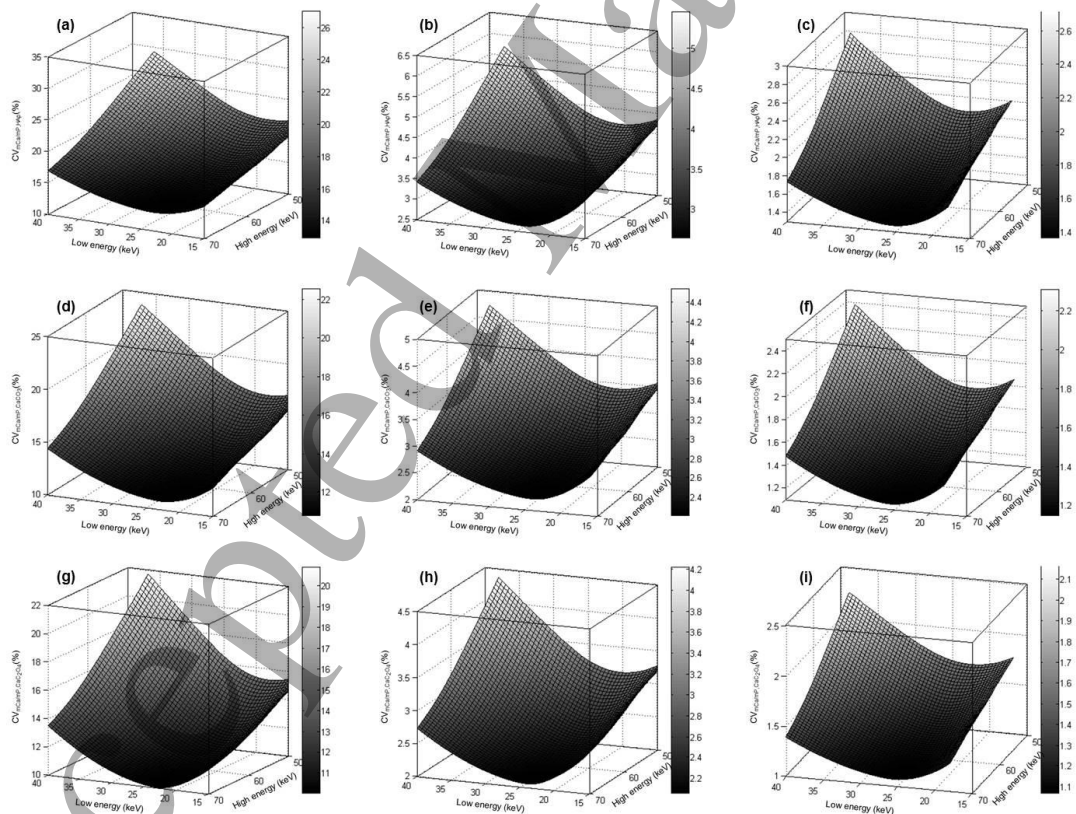


Figure 6. $CV_{mCa/mp,HAp}$ (%) (first row), $CV_{mCa/mp,CaCO_3}$ (%) (second row), and $CV_{mCa/mp,CaC_2O_4}$ (%) (third row) as a function of low- and high-energy for 100 μm (a,d,g), 500 μm (b,e,h) and 1000 μm (c,f,i) thicknesses.

3.1.2. Polyenergetic X-rays

3.1.2.1. Single exposure

Figure 7 shows the normalized spectra at 70 kV modified with Rh, Pd, Ag, Cd, Sn and I filters with thicknesses from 100 to 1000 μm , at 100 μm increments. These spectra were used as input data to the simulation of the current study, for the selection of filter material and thickness, as described below. Improved separation of the low- and high- energy bands can be achieved by all filter materials tested as the filter thickness increases. However, thicker filters lead to poor statistics due to the decreased number of photons.

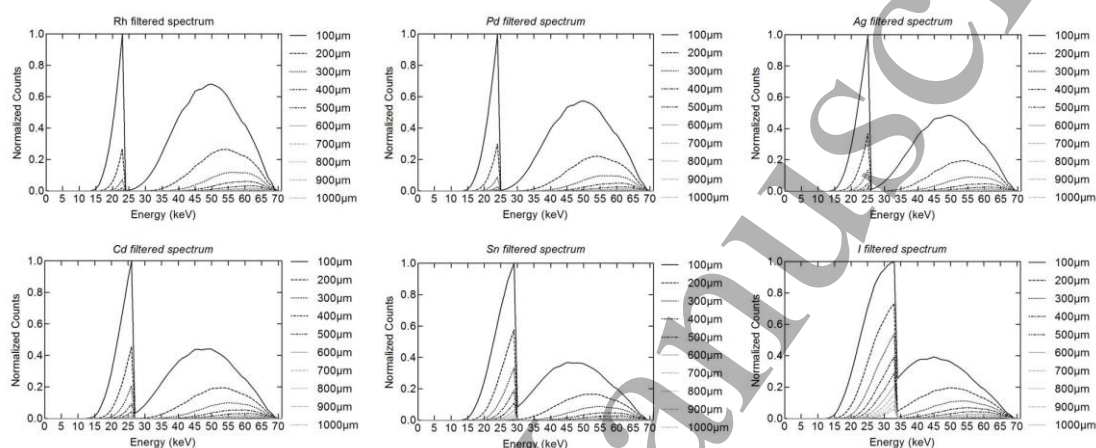


Figure 7. Filtered spectra with Rh, Pd, Ag, Cd, Sn and I with thicknesses from 100 to 1000 μm , in 100 μm increments, at 70 kV.

Figure 8 shows the mean energies for the low- and high-energy spectra filtered with Rh, Pd, Ag, Cd, Sn and I as a function of surface density (g/cm^2). Over the whole surface density range, only Ag and Cd filters have mean energies in the range indicated by the monoenergetic study. The dotted lines correspond to 23 and 27 keV, the lower and the upper limit for the low-energy indicated by the monoenergetic study.

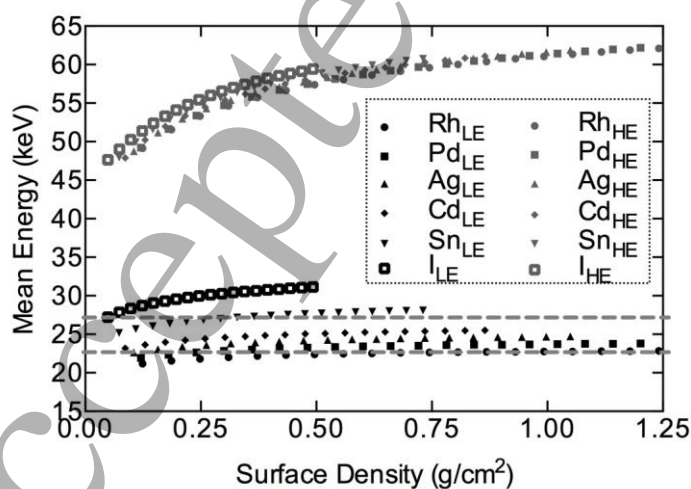


Figure 8. Low- and high-energy mean energies of Rh, Pd, Ag, Cd, Sn and I filtered spectra, as a function of filters' surface densities.

The averaged difference in mean energies of Ag and Cd filtered spectra was less than 0.6 and 0.8 keV for the low- and high-energy bands, respectively, across the examined surface density range. The Cd filter was selected, as it was available to our laboratory.

Figure 9 shows the $CV_{mCa/mP}$ (%) of 500, 618.58 and 1040.47 μm HAp, CaCO_3 and CaC_2O_4 , respectively, plotted as a function of examined Cd surface densities and entrance dose. For surface densities in the range of 0.22 to 0.39 g/cm^2 , the entrance doses are lower than the mammography acceptable levels (6 mGy), as shown by the dotted line (European Commission 2014), with relatively low $CV_{mCa/mP}$ (%) values (<7%). The Cd surface density that was selected for this study is 0.26 g/cm^2 , corresponding to a thickness of 300 μm . At this thickness, there is a compromise between low $CV_{mCa/mP}$ (%) and dose (3.29 mGy) values for all calcification types. The low- and high-mean energies are 24 keV and 55 keV, respectively.

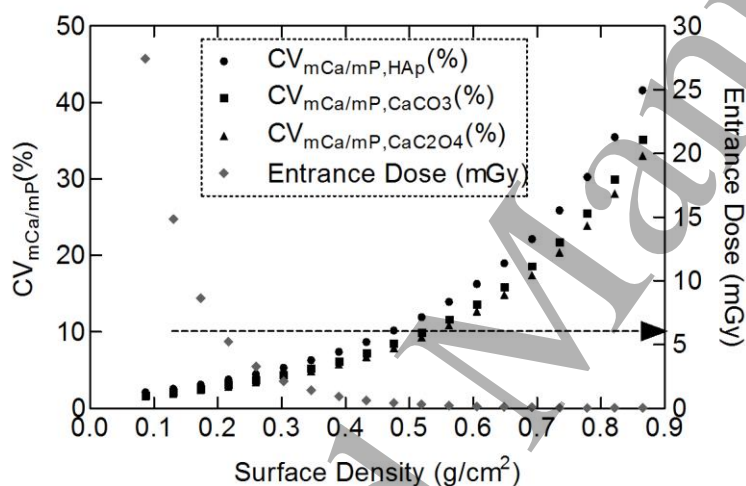


Figure 9. $CV_{mCa/mP, HAp}$ (%), $CV_{mCa/mP, CaCO_3}$ (%) and $CV_{mCa/mP, CaC_2O_4}$ (%) as a function of entrance dose and the examined Cd surface densities.

Figure 10 shows indicative probability distribution functions for 100 μm HAp, 123.72 μm CaCO_3 and 208.49 μm CaC_2O_4 . The HAp probability distribution function is plotted together with CaCO_3 (left) and CaC_2O_4 (right) probability distribution functions. The grey dashed lines indicate the intersection point of the probability distribution functions, separating the overlap area into the false negative (FN) and false positive (FP).

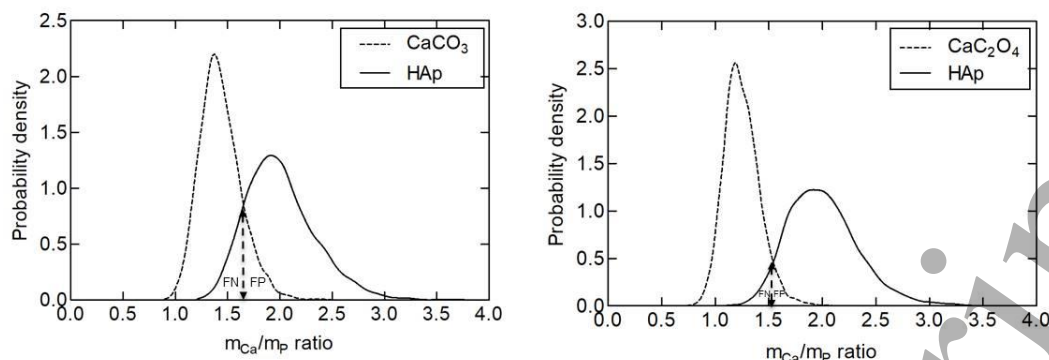


Figure 10. Indicative probability distribution functions for 100 μm HAp, 123.72 μm CaCO_3 and 208.49 μm CaC_2O_4 .

Table 2 shows the false negative (%) and false positive (%) values, as well as the overlap area (%), defined as the sum of these values, for the single exposure technique. The results presented here are for calcification thicknesses of 100, 300, 500, 700 and 900 μm HAp and the corresponding thicknesses for CaCO_3 and CaC_2O_4 and breast thicknesses of 4.2, 5 and 6 cm. For all breast thicknesses, the entrance dose was kept at 3.29 mGy. The $CV_{m_{\text{Ca}}/m_{\text{P}},\text{HAp}}(\%)$ for all examined calcification thicknesses ranged from: (i) 2.37 to 21.67% for 4.2 cm, (ii) 2.63 to 23.81% for 5 cm, and (iii) 3.02 to 26.92% for 6 cm. The $CV_{m_{\text{Ca}}/m_{\text{P}},\text{CaCO}_3}(\%)$ for all examined calcification thicknesses ranged from: (i) 1.95 to 17.83% for 4.2 cm, (ii) 2.17 to 19.60% for 5 cm, and (iii) 2.50 to 22.19% for 6 cm. The $CV_{m_{\text{Ca}}/m_{\text{P}},\text{CaC}_2\text{O}_4}(\%)$ for all examined calcification thicknesses ranged from: (i) 1.82 to 16.63% for 4.2 cm, (ii) 2.02 to 18.30% for 5 cm, and (iii) 2.32 to 20.73% for 6 cm.

Table 2. Overlap area-OA (%), false negative-FN (%) and false positive-FP (%) values for indicative thicknesses for the single exposure technique.

Case	t_{HAp} (μm)	T=4.2 cm			T=5 cm			T=6 cm		
		OA (%)	FN (%)	FP (%)	OA (%)	FN (%)	FP (%)	OA (%)	FN (%)	FP (%)
HAp; CaCO_3	100	79.82	40.94	38.88	82.90	43.40	39.50	98.99	2.89	96.10
	300	14.96	7.63	7.33	18.92	9.88	9.04	25.26	12.93	12.33
	500	1.82	0.92	0.90	3.29	1.65	1.64	6.29	3.19	3.10
	700	0.08	0.04	0.04	0.34	0.16	0.18	0.97	0.48	0.49
	900	0.00	0.00	0.00	0.01	0.01	0.00	0.08	0.04	0.04
HAp; CaC_2O_4	100	68.46	14.48	53.98	80.73	10.33	70.40	95.45	5.02	90.43
	300	3.18	1.56	1.62	5.27	2.73	2.54	8.77	4.43	4.34
	500	0.03	0.03	0.00	0.09	0.06	0.03	0.44	0.23	0.21
	700	0.00	0.00	0.00	0.00	0.00	0.00	0.00	0.00	0.00
	900	0.00	0.00	0.00	0.00	0.00	0.00	0.00	0.00	0.00

3.1.2.2. Double exposure

Figure 11 shows $CV_{m_{\text{Ca}}/m_{\text{P}},\text{HAp}}(\%)$, $CV_{m_{\text{Ca}}/m_{\text{P}},\text{CaCO}_3}(\%)$ and $CV_{m_{\text{Ca}}/m_{\text{P}},\text{CaC}_2\text{O}_4}(\%)$ for

500 μm HAp and the corresponding thicknesses for CaCO_3 and CaC_2O_4 , as a function of surface density (g/cm^2) for all the high-energy filters (Cu, Ho, Tm, and Lu), combined with a Cd filter of 100 μm thickness for the low-energy. Copper was selected as the high-energy filter due to its lower $CV_{m_{\text{Ca}/m_{\text{P}}}}$ (%) values compared to the other filters, for all calcification types.

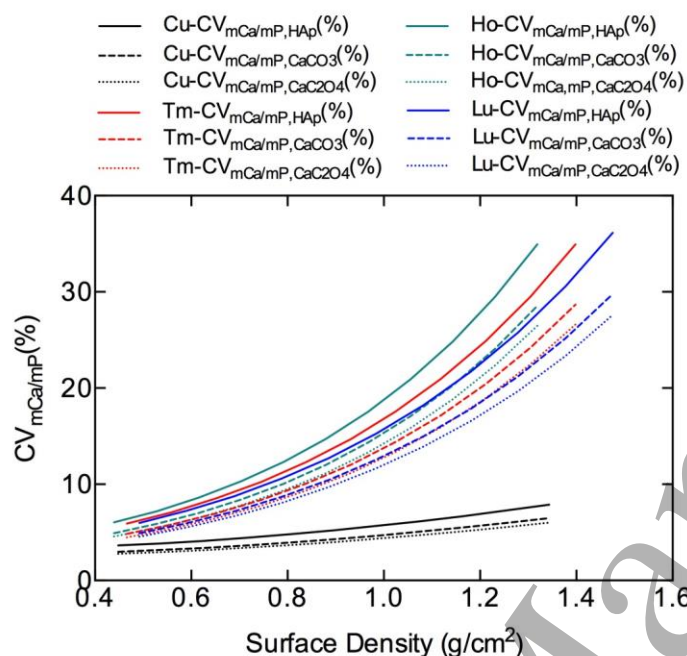


Figure 11. $CV_{m_{\text{Ca}/m_{\text{P}}},\text{HAp}}(\%)$, $CV_{m_{\text{Ca}/m_{\text{P}}},\text{CaCO}_3}(\%)$ and $CV_{m_{\text{Ca}/m_{\text{P}}},\text{CaC}_2\text{O}_4}(\%)$ as a function of surface density for all high-energy filters with 100 μm Cd (low-energy filter).

Figure 12 shows $CV_{m_{\text{Ca}/m_{\text{P}}},\text{HAp}}(\%)$, $CV_{m_{\text{Ca}/m_{\text{P}}},\text{CaCO}_3}(\%)$, $CV_{m_{\text{Ca}/m_{\text{P}}},\text{CaC}_2\text{O}_4}(\%)$ and entrance dose as a function of surface density (g/cm^2) of Cu combined with a Cd filter of 100 μm thickness. The $CV_{m_{\text{Ca}/m_{\text{P}}}}$ (%) data correspond to 500, 618.58 and 1040.47 μm HAp, CaCO_3 and CaC_2O_4 , respectively. For the whole surface density range, the entrance surface dose was within the acceptable levels (6 mGy). In order the entrance dose to be comparable with the single exposure method, 0.89 g/cm^2 surface density was selected, since it results in total entrance dose of 3.25 mGy.

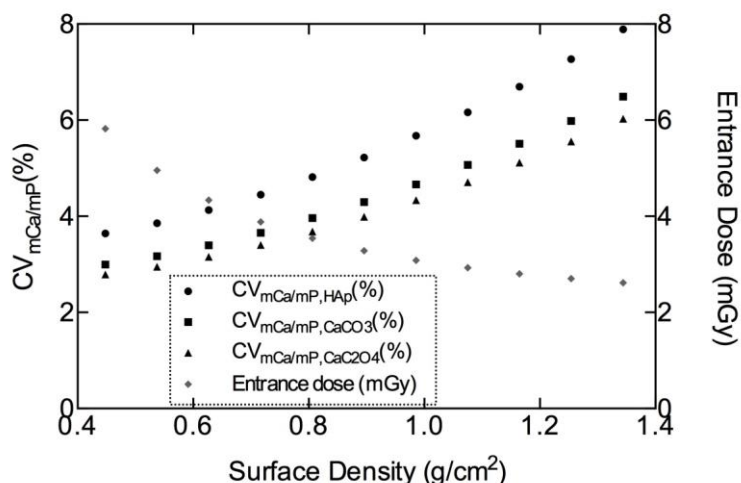


Figure 12. $CV_{mCa/mP,HAp}(\%)$, $CV_{mCa/mP,CaCO_3}(\%)$ and $CV_{mCa/mP,CaC_2O_4}(\%)$ as a function of surface density (g/cm^2) of Cu combined with a Cd filter of 100 μm thickness and entrance dose.

Table 3 shows the false negative (%), false positive (%) and overlap area (%) values for calcification thicknesses of 100, 300, 500, 700 and 900 μm HAp and the corresponding thicknesses for $CaCO_3$ and CaC_2O_4 and breast thicknesses of 4.2, 5 and 6 cm. The $CV_{mCa/mP,HAp}(\%)$ for all examined calcification thicknesses ranged from: (i) 2.71 to 25.51% for 4.2 cm, (ii) 2.97 to 27.81% for 5 cm, and (iii) 3.34 to 31.03% for 6 cm. The $CV_{mCa/mP,CaCO_3}(\%)$ for all examined calcification thicknesses ranged from: (i) 2.23 to 20.93% for 4.2 cm, (ii) 2.45 to 22.82% for 5 cm, and (iii) 2.75 to 25.49% for 6 cm. The $CV_{mCa/mP,CaC_2O_4}(\%)$ for all examined calcification thicknesses ranged from: (i) 2.07 to 19.51% for 4.2 cm, (ii) 2.27 to 21.28% for 5 cm, and (iii) 2.56 to 23.78% for 6 cm.

Table 3. Overlap area-OA (%), false negative-FN (%) and false positive-FP (%) values for indicative thicknesses for the double exposure technique.

Case	t_{HAp} (μm)	T=4.2 cm			T=5 cm			T=6 cm		
		OA (%)	FN (%)	FP (%)	OA (%)	FN (%)	FP (%)	OA (%)	FN (%)	FP (%)
HAp; $CaCO_3$	100	59.52	30.59	28.93	81.34	15.36	65.98	97.81	5.78	92.03
	300	12.15	5.91	6.24	15.05	7.58	7.47	20.22	10.18	10.04
	500	0.90	0.37	0.53	1.53	0.77	0.76	3.54	1.79	1.75
	700	0.00	0.00	0.00	0.00	0.00	0.00	0.27	0.17	0.10
	900	0.00	0.00	0.00	0.00	0.00	0.00	0.00	0.00	0.00
HAp; CaC_2O_4	100	42.07	20.86	21.21	52.08	21.18	30.90	91.55	26.33	65.22
	300	2.12	1.07	1.05	2.88	1.54	1.34	5.44	2.53	2.91
	500	0.00	0.00	0.00	0.01	0.00	0.01	0.05	0.02	0.03
	700	0.00	0.00	0.00	0.00	0.00	0.00	0.00	0.00	0.00
	900	0.00	0.00	0.00	0.00	0.00	0.00	0.00	0.00	0.00

3.2. Experimental evaluation of the method

3.2.1. Single exposure technique

The averaged m_{Ca}/m_P values for all thicknesses, the $CV_{m_{Ca}/m_P, meas}$ (%) and the results of Mann Whitney U test, for the examined calcification types and thicknesses are shown in table 4. The critical U value was 23 in all cases (Milton 1964), since each phantom was irradiated 10 times. The Mann Whitney U test showed that calcifications with thickness of 300 μm HAp or higher can be characterized.

Table 4. Averaged m_{Ca}/m_P for all thicknesses, $CV_{m_{Ca}/m_P, meas}$ (%) and Mann Whitney U test results of calcification phantoms for the single exposure technique.

t_{HAp} (μm)	m_{Ca}/m_P			$CV_{m_{Ca}/m_P, meas}$ (%)			Mann Whitney U test		
	HAp	CaCO ₃	CaC ₂ O ₄	HAp	CaCO ₃	CaC ₂ O ₄	HAp; CaCO ₃	HAp; CaC ₂ O ₄	Critical value
300				13.99	16.59	9.05	18	0	23
500	1.58	1.31	0.75	12.51	8.71	11.13	16	0	23
700				13.67	9.44	12.51	13	0	23
900				11.72	8.47	5.93	2	0	23

In figure 13 the averaged m_{Ca}/m_P values and the corresponding error bars are plotted, obtained from the simulation study and the experimental evaluation.

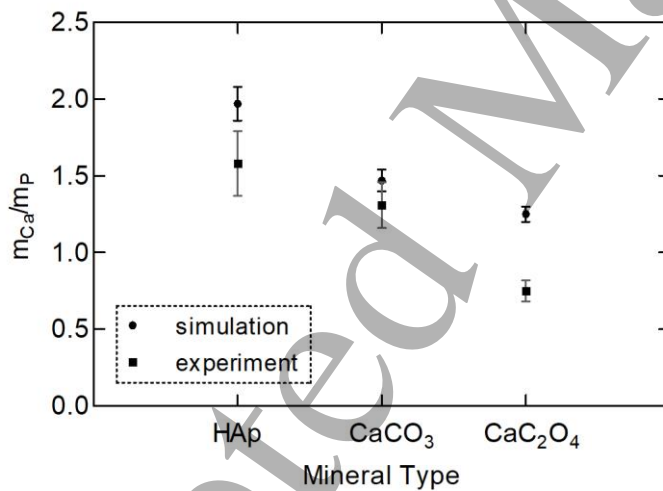


Figure 13. Averaged m_{Ca}/m_P values obtained from simulation and experimental studies for the single exposure technique.

3.2.2. Double exposure technique

The averaged m_{Ca}/m_P values for all thicknesses, the $CV_{m_{Ca}/m_P, meas}$ (%) of the measurements and the results of Mann Whitney U test for all calcification types, as well as, the examined thicknesses are shown in table 5. The critical U value was 127 in all cases (Milton 1964), as in each phantom 20 ROIs were selected. The Mann Whitney U test concluded that calcifications of 300 μm HAp thickness or higher can be characterized.

Table 5. Averaged m_{Ca}/m_P for all thicknesses, $CV_{m_{Ca}/m_P, meas}$ (%) and Mann Whitney U test results of calcification phantoms for the double exposure technique.

t_{HAp} (μm)	m_{Ca}/m_P			$CV_{m_{Ca}/m_P, meas}$ (%)			Mann Whitney U test		
	HAp	CaCO ₃	CaC ₂ O ₄	HAp	CaCO ₃	CaC ₂ O ₄	U value		Critical value
							HAp; CaCO ₃	HAp; CaC ₂ O ₄	
300				21.29	22.30	11.04	90	0	127
500	1.70	1.17	1.02	19.74	5.48	5.06	3	0	127
700				7.04	19.86	6.79	0	0	127
900				5.93	5.75	5.46	0	0	127

In figure 14 the averaged m_{Ca}/m_P values and the corresponding error bars are plotted, obtained from the simulation study and the experimental evaluation.

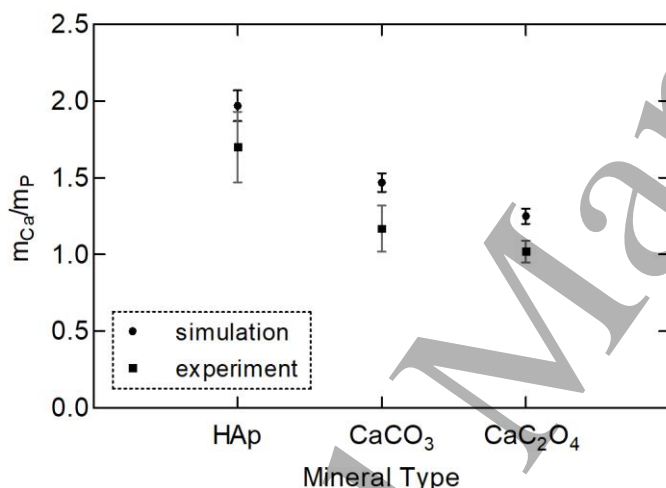


Figure 14. Averaged m_{Ca}/m_P values obtained from simulation and experimental studies for the double exposure technique.

4. Discussion

In this study, a dual energy method for the characterization of calcification minerals was developed, based on the determination of the effective Calcium/Phosphorus mass ratio (m_{Ca}/m_P). A simulation study was conducted, using monoenergetic beams, based on analytical modeling, in order to select the optimal low-/high-incident energies. Monochromatic beams are available from synchrotrons, which have been used in experiments for mammography in several studies demonstrating their advantages (Malliori *et al* 2012, Szafraniec *et al* 2015, Longo *et al* 2016). Due to the fact that in clinical practice X-ray tubes are widely used, an adjustment of the simulation study to polyenergetic spectra was conducted. Furthermore, the effect of breast thickness was examined, using the simulation study of polyenergetic X-rays. It was found that the overlap area increased, as the breast thickness increased. For instance, in the case of HAp;CaCO₃ and calcification thickness of 300 μm HAp, an average increase of approximately 67.69% was observed (68.86% for the

1
2
3 single exposure, 66.51% for the double exposure) by increasing the breast thickness from 4.2
4 to 6 cm. However, the overlap areas will decrease by applying appropriate entrance doses to
5 the examined breast thicknesses. This can be employed without significantly increasing the
6 risk to the patient relating to dose considering the following procedure: (i) the clinician will
7 be able to distinguish the calcifications that must be characterized after the low-energy
8 irradiation, (ii) the second irradiation with the high-energy can be restricted in a small area
9 including the calcification, resulting in reduced mean absorbed dose to the breast. These
10 irregular shaped irradiation fields could be more accurately defined by adopting the solution
11 of a dedicated multi-leaf collimator.

12 The optimized irradiation parameters obtained from the simulation study were used for the
13 experimental evaluation of the method. Both single and double exposure techniques were
14 studied and applied using photon counting energy dispersive and energy integrating detector.
15 The Mann-Whitney U non-parametric statistical test was applied to the measured m_{Ca}/m_P
16 values and showed that there are statistically significant differences ($p < 0.05$) between the
17 calcification minerals for thicknesses of 300 μm or higher, in both single and double
18 exposure techniques. In our method, cylindrical phantoms were irradiated in the longitudinal
19 direction where the thickness of the mineral was constant. For other shapes (spherical or
20 ellipsoidal) a mean thickness value lower than the maximum thickness that can be reached in
21 the beam path, must be considered.

22 In the polyenergetic studies, the mass attenuation coefficients were replaced by the effective
23 mass attenuation coefficients of each spectral peak of the simulated or measured filtered
24 spectra. The disadvantage of this approach is that neighboring energy pairs, which lead the
25 equation system (please see Appendix A1, A2, A3) to linear dependence, are not considered
26 in the simulation study. Furthermore, the determination of the effective mass attenuation
27 coefficients does not take into consideration the beam hardening effect of the polyenergetic
28 spectra. Additionally, the mass attenuation coefficient does not include the number of
29 scattered photons that can be finally found in the beam falling on the detector. However, in
30 both geometries of the experimental configurations (even in the pencil beam), after coherent
31 or incoherent interactions in matter, a number of photons can be detected. These reasons
32 explain (i) the higher measured $CV_{m_{Ca}/m_P, meas} (\%)$ compared to the theoretical
33 $CV_{m_{Ca}/m_P} (\%)$, and (ii) the systematic decrease in the m_{Ca}/m_P values that can be observed
34 in the experimental results compared to those obtained from the simulation, at both single and
35 double exposure techniques. Hence, a correction factor of approximately 1.35 and 1.21 can be
36 applied to the measured m_{Ca}/m_P values for the single and double exposure technique,
37 respectively, improving the accuracy of the method. Furthermore, the electronic and X-ray
38 source instability, which are not considered in the simulation study, led to the higher
39 measured $CV_{m_{Ca}/m_P, meas} (\%)$ compared to the theoretical $CV_{m_{Ca}/m_P} (\%)$. Comparing the
40 nominal m_{Ca}/m_P value of HAp 2.15 (Sotiropoulou *et al* 2015) with the measured for the
41 single 1.58 and the double 1.70 exposure technique, the calculated accuracy of the method
42 was 26.51% and 20.93%, respectively. The accuracy of the method can be improved by using
43 a calibration procedure incorporating inverse mapping techniques (Kappadath and Shaw
44 2003). When polynomial nonlinear inverse functions are applied, error parameters arising
45 from beam hardening, scatter radiation and nonlinear response of the detector, can be
46 diminished or even eliminated (Sotiropoulou *et al* 2016) and will be investigated in future
47 studies.

1
2
3
4
5
6
7
8
9
10
11
12
13
14
15
16
17
18
19
20
21
22
23
24
25
26
27
28
29
30
31
32
33
34
35
36
37
38
39
40
41
42
43
44
45
46
47
48
49
50
51
52
53
54
55
56
57
58
59
60

In the simulation study, the total number of photons after attenuation, in the single exposure technique was $\sim 2 \times 10^6 / 1.5 \times 10^7$ for the low-/high-energy, while in the double exposure technique was $\sim 3 \times 10^6 / 1.5 \times 10^7$ for the low-/high-energy. For the measured data to be consistent with the simulation, the measured number of photons was $\sim 1 \times 10^6 / 1 \times 10^7$ for the low-/high-energy, in the single exposure technique. The corresponding number of photons in the double exposure technique was $3 \times 10^6 / 1.3 \times 10^7$ per mm^2 for the low-/high-energy. The imaging detector has a pixel with an active area of $22.5 \times 22.5 \mu\text{m}^2$, thus approximately $44 \times 44 = 1,936$ pixels must be used in order to obtain 1 mm^2 corresponding to approximately 3×10^6 and 1.3×10^7 number of photons. The detector used has a bit depth (digital output) of 12 bits corresponding to 4,096 gray levels. Summing the events in the 1,936 number of pixels, the highest pixel value that can be achieved is $1,936 \times 4,096 = 7,929,856 \sim 8 \times 10^6$. Hence, ROIs of 44×44 pixels are adequate to obtain proper number of photons for the double exposure technique.

In commercially available clinical mammography systems the main restriction is that the X-ray source high voltage ranges from 20 to 49 kV. The low- and high-energy, indicated by the current monoenergetic simulation study, ranges from 23 to 27 keV and 53 to 70 keV, respectively. Thus, the adaptation of a clinical system, where the mean energy will be lower than 53 keV, will result in a $CV_{mCa/mP}$ (%) higher than that of +50% of the minimum $CV_{mCa/mP}$ (%) (Fig. 6). This will increase the minimum calcification thickness that can be characterized. The majority of the installed clinical detector systems have a minimum pixel size of $70 \mu\text{m}$ with a bit depth up to 14 bits corresponding to 16,384 gray levels. In order to characterize the mineral types, a number of photons of about 10^7 are essential. Summing the events in 225 number of pixels (ROI of 15×15 pixels in order to obtain 1 mm^2), the highest pixel value that can be achieved is $225 \times 16,384 = 3,686,400 \sim 3.7 \times 10^6$. Comparing this value with that of the detector used, only the half pixel values per area can be obtained from a detector of a clinical system.

A clinical system appropriate for this method would be a mammography system with W anode, high voltage generator ranging from 25 to 70 kV and a detector system with a combination of pixel size and depth capable of registering 10^7 photons per calcification area. For instance, if a calcification of $350 \mu\text{m}$ must be characterized and the pixel size is $70 \mu\text{m}$, the calcification will be spanned across $5 \times 5 = 25$ pixels. These pixels must be able to register 10^7 photons or 4×10^5 photons/pixel. In order to achieve that, a bit depth of 19 ($\log_2(4 \times 10^5) = 18.61$) is required. To summarize, the required bit depth (R_{bit}) can be expressed as $R_{bit} = \log_2(I \cdot PA/CA)$, where I is the required number of photons, PA and CA are the pixel and the calcification area, respectively.

The dual energy method implemented in this work discriminates calcifications thicker than $300 \mu\text{m}$, mainly due to the statistical noise which depends on the final detected number of photons. In breast, small microcalcification clusters, which are important for malignancy diagnosis, consist of numerous calcifications. If microcalcifications inside the cluster are thinner than $300 \mu\text{m}$, ROIs on the calcifications can be selected. By summing the corresponding photons from each ROI, the total number of photons will be increased potentially allowing the characterization of microcalcifications in the cluster. In future work, phantoms simulating realistic breast will be constructed using inhomogeneous breast tissue equivalent materials and calcifications with smaller sizes.

5. Conclusions

We proposed a dual energy method for the characterization of minerals associated with pathogenesis. The presented analytical model uses monoenergetic and polyenergetic X-ray beams to determine the m_{Ca}/m_P . The effective m_{Ca}/m_P is calculated for three calcification minerals, indicating malignancy (HAp) and benignancy ($CaCO_3$, CaC_2O_4). The experimental evaluation of the method revealed that calcifications of 300 μm HAp, and the corresponding calcification thicknesses for $CaCO_3$ and CaC_2O_4 , or higher can be characterized. Further studies will indicate the potential of the method to provide *in-vivo* information about the minerals avoiding invasive diagnostic methods such as biopsy.

Acknowledgements

The authors wish to thank Mr. I. Ntinou for his general statistical consulting. This work was supported by Grant E.040 from the Research Committee of the University of Patras (Programme K. Karatheodori).

Appendix: Ca/P mass ratio determination

Consider that along the radiation path, three major components can be regarded as attenuators: calcium-Ca, phosphate- PO_4 and breast tissue. The total thickness-T (cm) is given by:

$$T = t_{Ca} + t_{PO_4} + t_b \quad (A1)$$

where, t_{Ca} , t_{PO_4} , t_b are the thicknesses of calcium, phosphate and breast tissue respectively.

Using two monoenergetic X-rays, for the low- (l) and high-energy (h), and accepting an exponential attenuation of both X-rays, then the intensities with only the breast tissue in the radiation path (where $t_b = T$) can be obtained by:

$$I_{b,E_i} = I_{o,E_i} e^{-\mu_{b,E_i} T} \quad i=l,h \quad (A2)$$

where, I_{o,E_i} is the unattenuated intensity for the low- and high-energy, μ_{b,E_i} is the energy-dependent linear attenuation coefficient (1/cm) for breast tissue composed of 50% adipose and 50% glandular tissue ($0.5\mu_{a,E_i} + 0.5\mu_{g,E_i}$) and T is the total thickness (cm).

Respectively, when the three materials are present, the attenuated intensities for the low- and high-energy are given by:

$$I_{c,E_i} = I_{o,E_i} e^{-\mu_{Ca,E_i} t_{Ca} - \mu_{PO_4,E_i} t_{PO_4} - \mu_{b,E_i} t_b} \quad i=l,h \quad (A3)$$

where, I_{o,E_i} is the unattenuated intensity for the low- and high-energy and μ_{Ca,E_i} , μ_{PO_4,E_i} , μ_{b,E_i} are the energy-depended linear attenuation coefficients (1/cm) for calcium, phosphate and breast tissue, respectively.

Defining, $\Delta\mu_{Ca,E_i} = (\mu_{Ca,E_i} - \mu_{b,E_i})$ and $\Delta\mu_{PO_4,E_i} = (\mu_{PO_4,E_i} - \mu_{b,E_i})$, solving for t_b in Eq. A1 and replace in Eq. A3, the low- and high-energy intensities can be rewritten as:

$$I_{c,E_i} = I_{o,E_i} e^{-\Delta\mu_{Ca,E_i} t_{Ca} - \Delta\mu_{PO_4,E_i} t_{PO_4} - \mu_{b,E_i} T} \quad i = l, h \quad (A4)$$

The X-ray densities are defined as the logarithmic transform of Eqs. A2, A4 (Fountos *et al* 1997, Lemacks *et al* 2002):

$$Y_{E_i} = \ln \left(\frac{I_{b,E_i}}{I_{c,E_i}} \right) = \ln \left(\frac{I_{o,E_i} e^{-\mu_{b,E_i} T}}{I_{o,E_i} e^{-\Delta\mu_{Ca,E_i} t_{Ca} - \Delta\mu_{PO_4,E_i} t_{PO_4} - \mu_{b,E_i} T}} \right) = \ln \left(e^{\Delta\mu_{Ca,E_i} t_{Ca} + \Delta\mu_{PO_4,E_i} t_{PO_4}} \right) \quad (A5)$$

$i = l, h$

Finally, X-ray densities for the low- and high-energy, are a linear function of thicknesses t_{Ca} and t_{PO_4} :

$$Y_{E_l} = \Delta\mu_{Ca,E_l} t_{Ca} + \Delta\mu_{PO_4,E_l} t_{PO_4} \quad (A6a)$$

$$Y_{E_h} = \Delta\mu_{Ca,E_h} t_{Ca} + \Delta\mu_{PO_4,E_h} t_{PO_4} \quad (A6b)$$

The two equations above form a linear system of two equations with two unknown variables (t_{Ca} and t_{PO_4}). The two thicknesses are obtained by solving the linear system of Eqs. A6a, A6b with Cramer's rule using the determinants:

$$D = \begin{pmatrix} \Delta\mu_{Ca,E_l} & \Delta\mu_{PO_4,E_l} \\ \Delta\mu_{Ca,E_h} & \Delta\mu_{PO_4,E_h} \end{pmatrix} = \Delta\mu_{Ca,E_l} \Delta\mu_{PO_4,E_h} - \Delta\mu_{Ca,E_h} \Delta\mu_{PO_4,E_l} \quad (A7)$$

$$D_{t_{Ca}} = \begin{pmatrix} Y_{E_l} & \Delta\mu_{PO_4,E_l} \\ Y_{E_h} & \Delta\mu_{PO_4,E_h} \end{pmatrix} = Y_{E_l} \Delta\mu_{PO_4,E_h} - Y_{E_h} \Delta\mu_{PO_4,E_l} \quad (A8)$$

$$D_{t_{PO_4}} = \begin{pmatrix} \Delta\mu_{Ca,E_l} & Y_{E_l} \\ \Delta\mu_{Ca,E_h} & Y_{E_h} \end{pmatrix} = Y_{E_h} \Delta\mu_{Ca,E_l} - Y_{E_l} \Delta\mu_{Ca,E_h} \quad (A9)$$

The thicknesses t_{Ca} and t_{PO_4} are calculated by:

$$t_{Ca} = \frac{D_{t_{Ca}}}{D} \quad (A10a)$$

$$t_{PO_4} = \frac{D_{t_{PO_4}}}{D} \quad (A10b)$$

From Eqs. A10a, A10b, substituting from A7, A8, A9 we obtain the ratio:

$$\frac{t_{Ca}}{t_{PO_4}} = \frac{Y_{E_l} \Delta \mu_{PO_4, E_h} - Y_{E_h} \Delta \mu_{PO_4, E_l}}{Y_{E_h} \Delta \mu_{Ca, E_l} - Y_{E_l} \Delta \mu_{Ca, E_h}} \quad (A11)$$

If ρ_{CaPO_4} is the density of $Ca_{10-x}(PO_4)_6$ and ρ_{Ca} , ρ_{PO_4} , m_{Ca} , m_{PO_4} are the densities and masses of Ca and PO_4 respectively, then

$$\rho_{CaPO_4} = \frac{(m_{Ca} + m_{PO_4}) \rho_{Ca} \rho_{PO_4}}{m_{Ca} \rho_{PO_4} + m_{PO_4} \rho_{Ca}} \quad (A12)$$

where the volume that m specifies is the volume of the beam inside the material.

$$\frac{V_{Ca}}{V_{PO_4}} = \frac{m_{Ca} / \rho_{Ca}}{m_{PO_4} / \rho_{PO_4}} = \frac{m_{Ca} \rho_{PO_4}}{m_{PO_4} \rho_{Ca}} \quad (A13)$$

where V_{Ca} , V_{PO_4} are the volumes of Ca and PO_4 exposed to the beam.

But $V_{Ca} = S_{Ca} t_{Ca}$ (A14) and $V_{PO_4} = S_{PO_4} t_{PO_4}$ (A15) where S_{Ca} , S_{PO_4} are the surfaces of

Ca and PO_4 exposed to the beam. From Eqs. A13, A14 and A15 $\frac{S_{Ca} t_{Ca}}{S_{PO_4} t_{PO_4}} = \frac{m_{Ca} \rho_{PO_4}}{m_{PO_4} \rho_{Ca}}$

(A16), where $S_{Ca} = S_{PO_4}$ since both surfaces are exposed to the same beam. Finally,

$$\frac{t_{Ca}}{t_{PO_4}} = \frac{m_{Ca} \rho_{PO_4}}{m_{PO_4} \rho_{Ca}} \quad (A17). \text{ Because the molecular weight ratio } (PO_4/P = 3.0679), \text{ the weight}$$

ratio is given by $\frac{m_{Ca}}{m_P} = \frac{m_{Ca}}{m_{PO_4}} 3.0679$ (A18) (Fountos *et al* 1997). Combining Eqs. A11, A12,

A17 and A18:

$$\frac{m_{Ca}}{m_P} = \frac{Y_{E_l} \Delta \mu_{PO_4, E_h} - Y_{E_h} \Delta \mu_{PO_4, E_l}}{Y_{E_h} \Delta \mu_{Ca, E_l} - Y_{E_l} \Delta \mu_{Ca, E_h}} 3.0679 \quad (A19)$$

The standard deviation in m_{Ca}/m_P is obtained by partial differentiation of Eq. A19, assuming Poisson distribution for the incident beam. Therefore the coefficient of variation (CV), $CV_{m_{Ca}/m_P} (\%) = \left(\frac{SD_{m_{Ca}/m_P}}{\text{mean}_{m_{Ca}/m_P}} \right) 100$, derives from:

$$CV_{m_{Ca}/m_P}^2 = \left(\frac{1}{I_{b,E_l}} + \frac{1}{I_{c,E_l}} \right) \left(\frac{(\Delta\mu_{PO_4,E_h})^2}{(Y_{E_l}\Delta\mu_{PO_4,E_h} - Y_{E_h}\Delta\mu_{PO_4,E_l})^2} + \frac{(\Delta\mu_{Ca,E_h})^2}{(Y_{E_h}\Delta\mu_{Ca,E_l} - Y_{E_l}\Delta\mu_{Ca,E_h})^2} \right) 100^2$$

$$+ \left(\frac{1}{I_{b,E_h}} + \frac{1}{I_{c,E_h}} \right) \left(\frac{(\Delta\mu_{PO_4,E_l})^2}{(Y_{E_l}\Delta\mu_{PO_4,E_h} - Y_{E_h}\Delta\mu_{PO_4,E_l})^2} + \frac{(\Delta\mu_{Ca,E_l})^2}{(Y_{E_h}\Delta\mu_{Ca,E_l} - Y_{E_l}\Delta\mu_{Ca,E_h})^2} \right) 100^2$$
(A20)

In order to obtain the linear attenuation coefficients used in the above equations, the mass attenuation coefficients (μ/ρ) were multiplied by the density (ρ) of the appropriate material. The density values of adipose-0.93 g/cm³ and glandular-1.04 g/cm³ tissue (which compose the breast tissue) were obtained from published data (Hammerstein *et al* 1979). Since the main mass in hydroxyapatite molecules is Ca_{10-x}(PO₄)₆, instead of ρ_{CaPO_4} , the density of hydroxyapatite (bone ash) 3.18 g/cm³ can be used (Fountos *et al* 1997).

References

- American College of Radiology. ACR practice guideline for the performance of screening mammography. Reston, VA: American College of Radiology 2006 217-225
- Baker R, Matousek P, Ronayne K L, Parker A W, Rogers K and Stone N 2007 Depth profiling of calcifications in breast tissue using picosecond Kerr-gated Raman spectroscopy *Analyst* **132** 48-53
- Baker R, Rogers K D, Shepherd N and Stone N 2010 New relationships between breast microcalcifications and cancer *Br. J. Cancer.* **103** 1034-1039
- Boone J M and Seibert J A 1997 An accurate method for computer-generating tungsten anode x-ray spectra from 30 to 140 kV *Med. Phys.* **24** 1661-1670
- Bowman A W and Azzalini A 1997 Applied Smoothing Techniques for Data Analysis *New York: Oxford University Press Inc.*
- Brandan M and Ramirez V 2006 Evaluation of dual energy subtraction of digital mammography images under conditions found in a commercial unit *Phys. Med. Biol.* **51** 2307-2320
- Busing C M, Kepler U and Menges V 1981 Differences in microcalcification in breast tumors *Virchows Arch. [Pathol Anat]* **393** 307-313
- Byng J W, Mainprize J G and Yaffe M J 1998 X-ray characterization of breast phantom materials *Phys. Med. Biol.* **43** 1367-1377
- Chen X, Mou X and Zhang L 2008 Indicator and Calibration Material for Microcalcification in Dual-energy Mammography *Medical Biometrics 7th International Conference (ICMB 2008, Hong Kong, China) Lecture Notes in Computer Science* **4901** 265-272

- 1
2
3 Chen X, Nishikawa R M, Chan S, Lau B A, Zhang L and Mou X 2013 Algorithmic scatter
4 correction in dual-energy digital mammography *Med. Phys.* **40** 111919
5
6 Cox RF and Morgan P 2013 Microcalcifications in breast cancer: Lessons from physiological
7 mineralization *Bone* **53** 437-450
8
9 Del Lama L S, Cunha D M and Poletti M E 2016 Validation of a modified PENELOPE
10 Monte Carlo code for applications in digital and dual energy mammography. *Radiat. Phys.*
11 *Chem.* <http://dx.doi.org/10.1016/j.radphyschem.2016.03.004>.
12
13 Del Lama L S, Godeli J and Poletti M E 2016a Monte Carlo simulation studies for the
14 determination of microcalcification thickness and glandular ratio through dual energy
15 mammography. *Radiat. Phys. Chem.* [http://dx.doi.org/10.1016/j.radphyschem.](http://dx.doi.org/10.1016/j.radphyschem.2016.02.005)
16 [2016.02.005](http://dx.doi.org/10.1016/j.radphyschem.2016.02.005).
17
18 Del Medical Systems Group, Roselle, IL [Online]. Available from:
19 <http://www.delmedical.com>.
20
21 European Commission (EC). Diagnostic Reference Levels in Thirty-six European Countries,
22 Radiation Protection 180, Part 2, 2014.
23
24 Fandos-Morera A, Prats-Esteve M, Tura-Soteras J and Traveria-Cros A 1988 Breast tumors:
25 Composition of microcalcifications *Radiology* **169** 325-327
26
27 Fountos G, Yasumura S and Glaros D 1997. The skeletal calcium/phosphorus ratio: A new in
28 vivo method of determination *Med. Phys.* **24** 1303-1310
29
30 Frappart L *et al* 1984. Structure and composition of microcalcifications in benign and
31 malignant lesions of the breast: study by light microscopy, microprobe analysis, and X-ray
32 diffraction *Hum. Pathol.* **15** 880-889
33
34 Frappart L, Remy I, Lin HC, Bremond A, Raudrant D, Grousseau B and Vauzelle JL 1986
35 Different types of microcalcifications observed in breast pathology *Virchows Arch. A.* **410**
36 179-187
37
38 Gong J K, Arnold J S and Cohn S H 1964 The density of organic and volatile and non volatile
39 inorganic components of bone *Anatom. Rec.* **149** 319-324
40
41 Haka A S, Shafer-Peltier K E, Fitzmaurice M, Crowe J, Dasari R R and Feld M S 2002
42 Identifying microcalcifications in benign and malignant breast lesions by probing
43 differences in their chemical composition using Raman spectroscopy *Clin. Cancer Res.* **62**
44 5375-5380
45
46 Hammerstein G, Miller D, White D, Masterson M, Woodard H and Laughlin J 1979
47 Absorbed radiation dose in mammography *Radiology* **130** 485-491
48
49 Hubbell J H and Seltzer S M 1996 Tables of X-ray mass attenuation coefficients and mass
50 energy absorption coefficients 1 keV to 20MeV for elements Z=1 to 92 and 48 additional
51 substances of dosimetric interest. US Department of commerce NISTIR, 5632
52
53 Johns P C and Yaffe M J 1987 X-ray characterization of normal and neoplastic breast tissues
54 *Phys. Med. Biol.* **32** 675-695
55
56 Jones M C, Marron J S and Sheather S J 1996 A Brief Survey of Bandwidth Selection for
57 Density Estimation *J. Am. Stat. Assoc.* **91** 401-407
58
59 Kappadath S C and Shaw C C 2003 Dual-energy digital mammography: Calibration and
60 inverse-mapping techniques to estimate calcification thickness and glandular-tissue ratio
Med. Phys. **30** 1110-1117
Kappadath S C and Shaw C C 2004 Quantitative evaluation of dual-energy digital
mammography for calcification imaging *Phys. Med. Biol.* **49** 2563-2576
Kappadath S C and Shaw C C 2005 Dual-energy digital mammography for calcification
imaging: Scatter and nonuniformity corrections *Med. Phys.* **32** 3395-3408

- 1
2
3 Kappadath S C and Shaw C C 2008 Dual-energy digital mammography for calcification
4 imaging: noise reduction techniques *Phys. Med. Biol.* **53** 5421-5443
- 5
6 Kerssens M M, Matousek P, Rogers K and Stone N 2010 Towards a safe non-invasive
7 method for evaluation the carbonate substitution levels of hydroxyapatite (HAP) in micro-
8 calcifications found in breast tissue *Analyt* **135** 3156-3161
- 9
10 Koukou V, Martini N, Michail C, Sotiropoulou P, Fountzoula C, Kalyvas N, Kandarakis I,
11 Nikiforidis G and Fountos G 2015 Dual energy method for breast imaging: A simulation
12 study *Comput. Math. Methods Med.* 574238
- 13
14 Koukou V, Martini N, Fountos G, Michail C, Bakas A, Oikonomou G, Kandarakis I and
15 Nikiforidis G 2017 Application of a dual energy X-ray imaging method on breast
16 specimen *Results in Physics* **7** 1634-1636
- 17
18 Koukou V, Martini N, Fountos G, Michail C, Sotiropoulou P, Bakas A, Kalyvas N,
19 Kandarakis I, Speller D and Nikiforidis G 2017a Dual energy subtraction method for
20 breast calcification imaging *Nucl. Instrum. Meth. Phys. Res. A* **848** 31-38
- 21
22 Leborgne R 1951 Diagnosis of tumors of the breast by simple roentgenography;
23 Calcifications in carcinomas *Am. J. Roentgenol. Radium Ther. Nucl. Med.* **65** 1-11
- 24
25 Lemacks M R, Kappadath S C, Shaw C C, Liu X and Whitman G J 2002 A dual-energy
26 subtraction technique for microcalcification imaging in digital mammography- A signal-
27 to-noise analysis *Med. Phys.* **29** 1739-1751
- 28
29 Longo R *et al* 2016 Towards breast tomography with synchrotron radiation at Elettra: first
30 images *Phys. Med. Biol.* **61** 1634-1649
- 31
32 Malliori A, Bliznakova K, Speller R D, Horrocks J A, Rigon L, Tromba G and Pallikarakis N
33 2012 Image quality evaluation of breast tomosynthesis with synchrotron radiation *Med.*
34 *Phys.* **39** 5621-5634
- 35
36 Martini N, Koukou V, Michail C, Sotiropoulou P, Kalyvas N, Kandarakis I, Nikiforidis G and
37 Fountos G 2015 Pencil beam spectral measurements of Ce, Ho, Yb, and Ba powders for
38 potential use in medical applications *J. of Spectroscopy.* 563763
- 39
40 Matousek P and Stone N 2007 Prospects for the diagnosis of breast cancer by noninvasive
41 probing of calcifications using transmission Raman spectroscopy *J. Biomed. Opt.* **12**
42 024008
- 43
44 Matousek P and Stone N 2013 Recent advances in the development of Raman spectroscopy
45 for deep non-invasive medical diagnosis *J. Biophotonics.* **6** 7-19
- 46
47 Michail C, Fountos G, Valais I, Kalyvas N, Liaparinos P, Kandarakis I and Panayiotakis G
48 2011a Evaluation of the red emitting Gd₂O₂S:Eu powder scintillator for use in indirect X
49 ray digital mammography detectors *IEEE Trans. Nucl. Sci.* **58** 2503-2511
- 50
51 Michail C, Spyropoulou V, Fountos G, Kalyvas N, Valais I, Kandarakis I and Panayiotakis G
52 2011b Experimental and theoretical evaluation of a high resolution CMOS based detector
53 under X-ray imaging conditions *IEEE Trans. Nucl. Sci.* **58** 314-322
- 54
55 Milton R C 1964 An extended table of critical values for the Mann-Whitney (Wilcoxon) two-
56 sample statistic *J. Amer. Statist. Assoc.* **59** 925-934
- 57
58 Morgan M P, Cooke M M and McCarthy G M 2005 Microcalcifications Associated with
59 Breast Cancer: An Epiphenomenon or Biologically Significant Feature of Selected
60 Tumors? *J. Mammary Gland. Biol. Neoplasia* **10** 181-187
- Morgan M P, Cooke M M, Christopherson P A, Westfall P R and McCarthy G M 2001
Calcium hydroxyapatite promotes mitogenesis and matrix metalloproteinase expression in
human breast cancer cell lines *Mol. Carcinog.* **32** 111-117

- 1
2
3 Radi M J 1989 Calcium oxalate crystals in breast biopsies. An overlooked form of
4 microcalcification associated with benign breast disease *Arch. Pathol. Lab. Med.* **113**
5 1367-1369
6
7 Roberts M, Kahn E and Haddawy P 1995 Development of a Bayesian network for diagnosis
8 of breast cancer *IJCAI-95 Workshop on Building Probabilistic Networks*
9
10 Sorenson J A, Duke P R and Smith S W 1989 Simulation studies of dual-energy x-ray
11 absorptiometry *Med. Phys.* **16** 75-80
12
13 Sotiropoulou P, Fountos G, Martini N, Koukou V, Michail C, Kandarakis I and Nikiforidis G
14 2015 Bone calcium/phosphorus ratio determination using dual energy X-ray method *Phys.*
15 *Medica* **31** 307-313
16
17 Sotiropoulou P, Fountos G, Martini N, Koukou V, Michail C, Kandarakis I and Nikiforidis G
18 2016 Polynomial dual energy inverse functions for bone Calcium/Phosphorus ratio
19 determination and experimental evaluation *Appl. Radiat. Isot.* **118** 18-24
20
21 Stone N and Matousek P 2008 Advanced transmission Raman spectroscopy: a promising tool
22 for breast disease diagnosis *Cancer Res.* **68** 4424-4430
23
24 Stone N, Baker R, Rogers K, Parker A W and Matousek P 2007 Subsurface probing of
25 calcifications with spatially offset Raman spectroscopy (SORS): future possibilities for the
26 diagnosis of breast cancer *Analyst* **132** 899-905
27
28 Szafraniec M B *et al* 2015 Synchrotron based planar imaging and digital tomosynthesis of
29 breast and biopsy phantoms using a CMOS active pixel sensor. *Phys. Medica* **31** 192-198
30
31 Taibi A, Fabbri S, Baldelli P, di Maggio C, Gennaro G, Marziani M, Tuffanelli A and
32 Gambaccini M 2003 Dual-energy imaging in full-field digital mammography: a phantom
33 study *Phys. Med. Biol.* **48** 1945-1956
34
35 Wang Z, Hauser N, Singer G, Trippel M, Kubik-Huch R A, Chneider C W and Stampanoni
36 M 2014 Non-invasive classification of microcalcifications with phase-contrast X-ray
37 mammography *Nat. Commun.* **5** 1-9
38
39 Warren L M, Mackenzie A, Dance D R and Young K C 2013 Comparison of the x-ray
40 attenuation properties of breast calcifications, aluminum, hydroxyapatite and calcium
41 oxalate *Phys. Med. Biol.* **58** N103-N113
42
43 World Health Organization. World Health Statistics 2008; 2008
44
45
46
47
48
49
50
51
52
53
54
55
56
57
58
59
60